Piezoelectric coefficients and spontaneous polarization of ScAlN

Miguel A. Caro,[1,2,*] Siyuan Zhang,[3] Tommi Riekkinen,[4] Markku Ylilammi,[4] Michelle A. Moram,[3,5] Olga Lopez-Acevedo,[2] Jyrki Molarius,[4] and Tomi Laurila[1]

[1] *Department of Electrical Enegineering and Automation, Aalto University, Espoo, Finland*
[2] *COMP Centre of Excellence in Computational Nanoscience, Department of Applied Physics, Aalto University, Espoo, Finland*
[3] *Department of Materials Science and Metallurgy, University of Cambridge, Charles Babbage Road, CB3 0FS Cambridge, United Kingdom*
[4] *VTT Technical Research Centre of Finland, P.O. Box 1000, FI-02044 VTT, Finland*
[5] *Department of Materials, Imperial College London, Exhibition Road, SW7 2AZ London, United Kingdom*

(Dated: August 28, 2015)

We present a computational study of spontaneous polarization and piezoelectricity in $Sc_xAl_{1-x}N$ alloys in the compositional range from $x = 0$ to $x = 0.5$, obtained in the context of density functional theory and the Berry-phase theory of electric polarization using large periodic supercells. We report composition-dependent values of piezoelectric coefficients e_{ij}, piezoelectric moduli d_{ij} and elastic constants C_{ij}. The theoretical findings are complemented with experimental measurement of e_{33} for a series of sputtered ScAlN films carried out with a piezoelectric resonator. The rapid increase with Sc content of the piezoelectric response reported in previous studies is confirmed for the available data. A detailed description of the full methodology required to calculate the piezoelectric properties of ScAlN, with application to other complex alloys, is presented. In particular, we find that the large amount of internal strain present in ScAlN and its intricate relation with electric polarization make configurational sampling and the use of large supercells at different compositions necessary in order to accurately derive the piezoelectric response of the material.

I. INTRODUCTION

ScAlN is an emerging semiconductor material with potential applications in optics and electronics due to its unique properties. It can be integrated with conventional group-III nitrides, which are extremely important materials in the context of the lighting industry and other emerging applications,[1,2] in order to improve device performance.[3,4] In addition, AlN is CMOS-compatible and elements based on ScAlN could potentially be used in integrated circuits. The rapid enhancement of the piezoelectric (PZ) response of ScAlN compared to bulk AlN as the Sc fraction increases, together with its high Curie temperature, makes it interesting for use in PZ devices.[5] Since the first experimental evidence of this enhanced PZ behavior by Akiyama *et al.* in 2009,[5] a number of experimental[6–8] and theoretical[7,9] studies have confirmed this result, and the research in ScAlN for PZ applications has gathered pace.

Reliable material parameters are critical in device modeling and characterization. However, the accurate experimental determination of PZ constants of ScAlN is hindered by several factors, in particular the ability to grow high-quality single-phase films using sputtering techniques.[10] Also, a full set of PZ coefficients e_{ij} and PZ moduli d_{ij} for ScAlN is somewhat lacking from the literature. In the case of spontaneous polarization, experimental measurement is simply too challenging.

In the present paper we present a consistent set of composition-dependent PZ parameters for $Sc_xAl_{1-x}N$ in the range from $x = 0$ to $x = 0.5$ derived from density functional theory[11,12] (DFT) calculations using large periodic supercells and the Berry-phase theory of polarization.[13,14] We report PZ coefficients $e_{15}(x)$, $e_{31}(x)$ and $e_{33}(x)$, PZ moduli $d_{15}(x)$, $d_{31}(x)$ and $d_{33}(x)$, and spontaneous polarization $P_{\mathrm{SP}}(x)$. We compare these values to experimental and theoretical data available from the literature and add an own set of experimental values of e_{33} obtained with a bulk acoustic wave (BAW) resonator setup and sputtered ScAlN films. In addition, we provide a full set of composition-dependent elastic constants $C_{11}(x)$, $C_{12}(x)$, $C_{13}(x)$, $C_{33}(x)$ and $C_{44}(x)$ fully consistent with our methodology for PZ coefficients. We thoroughly discuss the complete theoretical methodology employed, its shortcomings and challenges. This detailed description can now guide the calculation of PZ properties of other complex piezoelectric alloys.

The paper is structured as follows. Sec. II describes the whole simulation procedure: Sec. II A deals with the choice of supercell, and is complemented by the Appendix; Sec. II B introduces the calculation details, including some practicalities related to the Berry-phase formalism; Sec. II C relates the procedure needed to retrieve the hexagonal PZ tensor from the triclinic supercell calculations; Sec. II D gives the spontaneous polarization results and details the strategy needed to compute it; Sec. II E contains the main results of the paper, the composition-dependent expressions for the PZ coefficients of ScAlN; Sec. II F deals with the transformation between PZ coefficients e_{ij} and PZ moduli d_{ij} and gives composition-dependent expressions for d_{ij} and the elastic constants C_{ij}. In Sec. III we explain the experimental procedure carried out to determine the values of e_{33} for a series of ScAlN films. Finally, in Sec. IV we discuss our

results and present our conclusions.

II. SIMULATION

There are several practical complications associated with the calculation of PZ constants and spontaneous polarization of crystalline solids. The formal theoretical framework to carry out this kind of calculation, in particular (but not limited to) in the context of *ab initio* methods, is known as the modern –or Berry-phase– theory of polarization, and was not developed until the early 1990s. A good account of this technique is available in the seminal papers by Vanderbilt and King-Smith,[13,14] the early review by Resta[15] and, more pedagogically, in a recent book chapter by Resta and Vanderbilt.[16] The Berry-phase approach has been successfully employed to calculate polarization values in technologically important materials, notably "traditional" nitrides (GaN, InN and AlN).[17] More recently, also studies of ScAlN have relied on this technique to calculate the e_{33} PZ coefficient.[9] The scope of the present work poses, however, additional difficulties owing to the huge internal strain present in ScAlN, which makes its structure largely deviate from a true wurtzite crystal. Calculation of spontaneous polarization and all of the PZ constants of ScAlN through the whole compositional regime requires a very careful study of configurational (alloy) effects on the results. In this section we describe this process in detail. Section II A deals with the finite supercell representation of the macroscopic alloy. In Sec. II B we provide the numerical details of the DFT and Berry-phase calculations. We discuss the implications of using triclinic supercells and how to deal with them in Sec. II C. Finally, Secs. II D, II E and II F present the computational results and discussion of spontaneous polarization, PZ coefficients and PZ moduli, respectively.

A. Supercell choice: random and quasirandom structures

In this study, the representation of realistic ScAlN alloys is carried out using periodic supercells containing 128 atoms, 64 cations (Sc or Al) and 64 N atoms, in a construction of $4\times4\times2$ wurtzite primitive unit cells (each containing 4 atoms). The different compositional regimes are achieved by replacing the corresponding number of Al atoms by Sc atoms in the cation sublattice. Although the supercells used are considerably large, the effect of configurational disorder is observed to affect the results, as will be shown later on. We therefore study different ways to obtain the macroscopically-averaged values of spontaneous polarization and piezoelectric tensor through the use of random and quasirandom supercells. To ensure that finite-size effects related to periodicity are minimized, randomly populated supercells are observed to be required. We also explore the degree of applicability of the special quasirandom structure (SQS) approach, which consists in placing the different atoms in optimal lattice sites such that the pair-correlation function (or other properties) of the periodic system resembles that of a random alloy as closely as possible.[18] Different optimizations methods for SQS cells have been studied, using two series of SQSs: those used by Zhang *et al.*[19] in previous work, that we refer to by "SQS#1", and a new series "SQS#2" at 12.5%, 25%, 37.5% and 50% Sc content, which were further optimized to yield zero pair-correlation coefficients up to bigger pair distances for the supercell size employed (128 atoms). We observe that SQSs are not as well suited for the representation of average piezoelectric properties of ScAlN alloys as they are for other properties, for instance elasticity. This trend suggests a strong fluctuation of the local piezoelectric properties of ScAlN at the microscopic scale, in line with (but stronger than) the local effects predicted for the related nitride alloy InGaN.[20] A more detailed analysis, presented in the Appendix, reveals that there appears to be no obvious correlation between supercell "randomness" (in the sense of calculated pair-correlation coefficients) and closeness of the supercell's piezoelectric coefficients to the configurational average.

B. Calculation details

Structural properties (lattice vectors and atomic positions) and self-consistent wave functions for the chosen ScAlN supercells are obtained within the framework of density functional theory (DFT)[11,12] as implemented in the VASP package[21,22] in the context of the projector augmented wave (PAW) method.[23,24] Together with the three outermost valence electrons of Sc ($4s^2 3d$), the semicore $3s$ and $3p$ electronic states were also explicitly included as valence states. For the exchange-correlation part of the total energy, the gradient-corrected functional of Perdew, Burke and Ernzerhof (PBE)[25] was used. The k-point sampling in the first Brillouin zone is done using a $2\times2\times2$ Monkhorst-Pack grid[26] centered at Γ. The plane wave cutoff was set to 600 eV. Such a high cutoff is needed in order to correctly describe internal strain in wurtzite nitrides,[27–29] which has a large impact on piezoelectric and spontaneous polarization.[20] The calculation of the electric polarization was carried out following the directives of the modern (or Berry-phase) theory of polarization,[13–15] using Martijn Marsman's implementation of this method as available in VASP.

To calculate the electric polarization a reference state of well-defined polarization is needed.[16] In the case of wurtzite materials, a straight-forward reference is the closely-related centrosymmetric (unstrained) zinc blende (ZB) lattice. In the case of the in-plane components of the polarization vector the unstrained WZ configuration can also be used: the polarization components vanish by symmetry along the c plane in unstrained wurtzite. Fig. 1 depicts the workflow that leads to the calculation

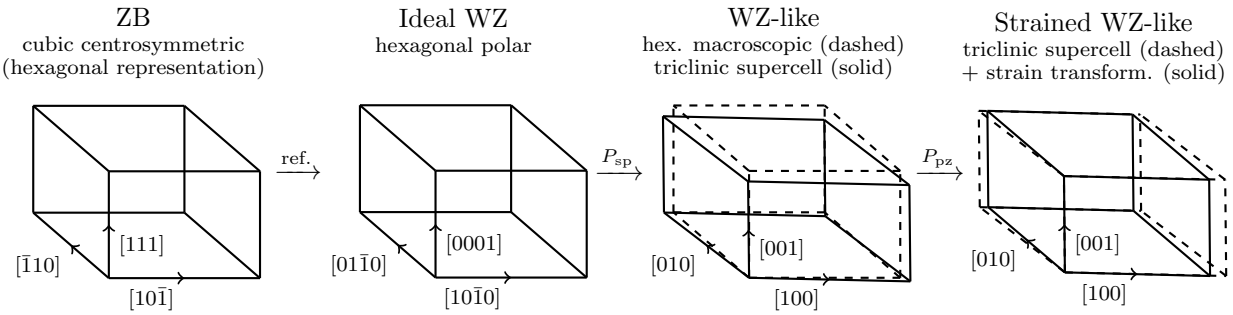

FIG. 1. Successive transformations needed in order to calculate spontaneous and piezoelectric polarization in a wurtzite-like material.

of the PZ tensor through the different steps involved: i) the ZB structure allows to establish a zero-polarization reference; ii) the ideal WZ structure serves in order to obtain the offset corrections to electronic and ionic polarizations (see next paragraph); iii) the evolution of the polarization from ideal WZ to the WZ-like relaxed structures gives the value of the spontaneous polarization; iv) the variation of the polarization upon small deformations of the relaxed structures enables the calculation of the piezoelectric tensor. In practice (the present case with hexagonal supercells, for instance), the ideal WZ supercell might sometimes lead to straight-forward polarization offsets and the first step (ZB calculation) may be skipped under those circumstances. Note that although ScAlN alloys are macroscopically hexagonal, a finite-size supercell will in general be triclinic, with lattice vectors similar, but not equal, to those of the hexagonal supercell, as shown in Fig. 1.

A complication associated to the Berry-phase approach stems from the choice of origin and the existence of the quantum of polarization when computing the electronic contribution to the electric polarization. The issue with the choice of origin is also present when computing the ionic part of the polarization.[13] These lead to offsets in the polarization values calculated directly, that must be subtracted before the physically-meaningful result can be obtained. However, if the origin to compute the polarization vector is chosen carefully, one can obtain simple expressions for the polarization offset as fractional multiples of the lattice vectors.[30] Given the lattice vectors of the ideal WZ supercells employed in this work:

$$\mathbf{a} = 4\,(a_0, 0, 0)\,, \qquad \mathbf{b} = 4\left(-\frac{a_0}{2}, \frac{\sqrt{3}a_0}{2}, 0\right),$$
$$\mathbf{c} = 2\,(0, 0, c_0)\,, \tag{1}$$

when the origin for computing the supercell's dipole moment is taken at $(0, 0, 0)$, in the specific case of a pure $Al_{64}N_{64}$ supercell, the calculation leads to the following offsets for the electronic and ionic parts of the dipole moment vector:

$$\mathbf{p}_0^{\text{ele}} = \frac{2e}{3}\mathbf{a} - \frac{2e}{3}\mathbf{b} + 0\mathbf{c},$$
$$\mathbf{p}_0^{\text{ion}} = \frac{640e}{3}\mathbf{a} + \frac{704e}{3}\mathbf{b} + 252e\mathbf{c}, \tag{2}$$

where e is the elementary charge. The strain dependence of the lattice vectors is inherited by the dipole moment and it must be taken into account when correcting the polarization results. Different (although similar) offsets are obtained for the ScAlN supercells because of having considered 11 valence electrons for Sc (including 8 semicore electrons). Otherwise, having considered only 3 valence electrons for Sc, the offsets would be identical.

C. Symmetry considerations

The use of supercells in theoretical calculations of alloyed compounds imposes a number of drawbacks. The most immediate consequence is that macroscopic properties of a material which lacks full periodicity (e.g. any disordered alloy) cannot be reproduced exactly with finite-size periodic structures. To minimize this problem one must rely, on the one hand, on supercells which are as large as computationally affordable and, on the other hand, configurational sampling of different supercells with the same composition. This combined strategy allows to both better represent the different microscopic configurations found in the macroscopic alloy and to remove the effect of spurious periodicity effects introduced by the supercell's geometry. In the case of ScAlN alloys, the large amount of internal strain does indeed lead to important deviations from hexagonal symmetry for relaxed supercells. This is even true for supercells containing as many as 128 atoms, as is presently the case.

Therefore, one is left dealing with supercells that have in general triclinic symmetry, i.e. no symmetry at all, and correspondingly complicated triclinic material tensors. In the case of the piezoelectric tensor, this means dealing with 18 independent piezoelectric coefficients e_{ij} rather than the three independent WZ coefficients e_{15}, e_{31} and e_{33}.[31] The implications might be better understood when these tensors are written down side by side

in matrix representation. The supercell's PZ tensor has the form:

$$e^{\text{tric}} = \begin{pmatrix} e_{11} & e_{12} & e_{13} & e_{14} & e_{15} & e_{16} \\ e_{21} & e_{22} & e_{23} & e_{24} & e_{25} & e_{26} \\ e_{31} & e_{32} & e_{33} & e_{34} & e_{35} & e_{36} \end{pmatrix}, \tag{3}$$

while the macroscopic alloy's PZ tensor has the form:[31]

$$e^{\text{hex}} = \begin{pmatrix} 0 & 0 & 0 & 0 & e_{15} & 0 \\ 0 & 0 & 0 & e_{15} & 0 & 0 \\ e_{31} & e_{31} & e_{33} & 0 & 0 & 0 \end{pmatrix}. \tag{4}$$

Similarly, the corresponding supercell's SP polarization will not be directed exactly parallel to the hexagonal [0001] direction (or c axis). Instead, it will point along some direction close to the triclinic [001], since the triclinic cell was obtained as a modification of an input hexagonal one (Fig. 1).

In order to retrieve the macroscopic material tensor from the supercell results, one can resort to the method proposed by Moakher and Norris,[32] whereby auxiliary *projectors* P^{sym} are used to "project" low symmetry tensors (triclinic in the present case) onto a higher symmetry tensor (hexagonal here) such that the Euclidean distance between the two tensors is minimized. In this context, one can obtain the "closest" hexagonal tensor to the original triclinic one. Moakher and Norris presented their method for analysis of elastic tensors (rank 4), which has already been used by Zhang *et al.*[33] to study elastic constants of ScAlN. It can however also be used to study lower (or higher) rank tensors, such as the PZ tensor (which has rank 3), provided that the appropriate projector is available. We have obtained this projector following Moakher and Norris's recipe.[32] One starts by expressing the PZ tensor as an 18-dimensional vector, with corresponding normalizing coefficients to preserve the Euclidean norm:

$$\begin{aligned} \mathbb{e}^{\text{tric}} \equiv \big(&e_{11}, e_{12}, e_{13}, \sqrt{2}e_{14}, \sqrt{2}e_{15}, \sqrt{2}e_{16}, e_{21}, e_{22}, e_{23}, \\ &\sqrt{2}e_{24}, \sqrt{2}e_{25}, \sqrt{2}e_{26}, e_{31}, e_{32}, e_{33}, \sqrt{2}e_{34}, \sqrt{2}e_{35}, \\ &\sqrt{2}e_{36}\big). \end{aligned} \tag{5}$$

The hexagonal version of Eq. (5) would then be

$$\begin{aligned} \mathbb{e}^{\text{hex}} \equiv \big(&0, 0, 0, 0, \sqrt{2}e_{15}, 0, 0, 0, 0, \sqrt{2}e_{15}, 0, 0, e_{31}, e_{31}, \\ &e_{33}, 0, 0, 0\big), \end{aligned} \tag{6}$$

which can be expanded in the basis $\left\{\mathbb{V}_i^{\text{hex}}\right\}$, that has the following three components:

$$\begin{aligned} \mathbb{V}_1^{\text{hex}} =& \frac{1}{\sqrt{2}}\left(0,0,0,0,1,0,0,0,0,0,1,0,0,0,0,0,0,0\right), \\ \mathbb{V}_2^{\text{hex}} =& \frac{1}{\sqrt{2}}\left(0,0,0,0,0,0,0,0,0,0,0,0,0,1,1,0,0,0\right), \\ \mathbb{V}_3^{\text{hex}} =& \left(0,0,0,0,0,0,0,0,0,0,0,0,0,0,0,1,0,0\right). \end{aligned} \tag{7}$$

Following Moakher and Norris,[32] P^{hex} for the PZ tensor is then:

$$P^{\text{hex}} = \sum_{i,j}^{N} \left(D^{-1}\right)_{ij} \mathbb{V}_i^{\text{hex}} \times \mathbb{V}_j^{\text{hex}}, \tag{8}$$

with $(D)_{ij} = \langle \mathbb{V}_i^{\text{hex}}, \mathbb{V}_j^{\text{hex}} \rangle$ being the elements of matrix D, and where $\langle , \rangle$ denotes inner product and $\times$ denotes outer product. N is the size of the basis, $N = 3$ in this case. The result is a sparse matrix of dimension 18×18:

$$P^{\text{hex}} = \left(\begin{array}{cccc|ccccc} 0_{4\times4} & \cdots & \cdots & 0_{1\times4} & & & & & \\ \vdots & \frac{1}{2} & \vdots & \frac{1}{2} & & & 0_{8\times10} & & \\ \vdots & \cdots & 0_{4\times4} & \cdots & & & & & \\ 0_{4\times1} & \frac{1}{2} & \vdots & \frac{1}{2} & & & & & \\ \hline & & & & 0_{2\times2} & \cdots & \cdots & \cdots & 0_{3\times2} \\ & & & & \vdots & \frac{1}{2} & \frac{1}{2} & 0 & \vdots \\ & 0_{10\times8} & & & \vdots & \frac{1}{2} & \frac{1}{2} & 0 & \vdots \\ & & & & \vdots & 0 & 0 & 1 & \vdots \\ & & & & 0_{2\times3} & \cdots & \cdots & \cdots & 0_{3\times3} \end{array}\right). \tag{9}$$

The hexagonal projection of $\mathbb{e}^{\text{tric}}$ is then

$$\begin{aligned} P^{\text{hex}}\mathbb{e}^{\text{tric}} = \Big(&0,0,0,0,0,\frac{e_{15}+e_{24}}{\sqrt{2}},0,0,0,0,0,\frac{e_{15}+e_{24}}{\sqrt{2}},0,0, \\ &\frac{e_{31}+e_{32}}{2},\frac{e_{31}+e_{32}}{2},e_{33},0,0,0\Big). \end{aligned} \tag{10}$$

Note that in general, due to the arbitrariness of choosing a specific set of Cartesian axes as reference frame for the triclinic cell, the rotational degrees of freedom also need to be taken into account when optimizing the projection. This means that a general rotation of the triclinic PZ tensor around the coordinate Cartesian axes (denoted by $R(\theta_x, \theta_y, \theta_z)$) needs to be performed before minimizing the Euclidean distance between $\mathbb{e}^{\text{tric}}$ and its hexagonal projection. The numerical optimization problem is then

$$\frac{\partial}{\partial\theta_i}\|R(\theta_x,\theta_y,\theta_z)\mathbb{e}^{\text{tric}} - P^{\text{hex}}R(\theta_x,\theta_y,\theta_z)\mathbb{e}^{\text{tric}}\|^2 = 0. \tag{11}$$

The reader is referred to Ref. 34 for further details.

In the case of the spontaneous polarization, it is straightforward to see that the optimized hexagonal projection of the SP polarization vector after rotating the triclinic value is simply minus its norm.[35]

D. Results: spontaneous polarization

The calculation of the spontaneous (SP) polarization is done, as outlined in Sec. II B, by studying the evolution

of the polarization vector as the structure is transformed from ideal WZ (internal parameter set to $u = \frac{3}{8}$) to the WZ-like ScAlN equilibrium structure. The ionic part of the polarization can be calculated in a straightforward manner, once the offsets are known and subtracted (e.g. Eq. (2)), as the difference between the ionic polarization of the relaxed structure and the reference ideal WZ (which is zero):

$$P^{\text{ion}}_{i,\text{SP}} = P^{\text{ion}}_{i,\text{tric}} - P^{\text{ion}}_{i,\text{idWZ}}, \tag{12}$$

where tric and idWZ denote the triclinic and ideal WZ supercell values, respectively, and i runs over each Cartesian component. For simplicity, we refrain from explicitly including the offset corrections in the equations for the ionic polarization, since they maintain their functional dependence on the lattice vectors throughout the transformation. This is true as long as the periodic replicas chosen to calculate the polarization are always the same. While the *ionic* polarization offset for a given structure is fully determined by the choice of origin, in the case of the *electronic* polarization this offset is also influenced by the *quantum of polarization*.[15,16] Since the Berry phase is an angular variable, well-defined only modulo 2π, large changes in its value corresponding to large changes in the sample's dipole moment may lead to ambiguous results. The total dipole moment of the supercell scales linearly with the number of primitive unit cells N_{cells} considered, whereas the length of the lattice vectors scales only as $N^{1/3}_{\text{cells}}$. Since the quantum of polarization ambiguity is related to lattice translations, this means that the "jumps" in the electronic polarization components are more likely to be observed as the supercell size grows larger. For our 128-atom supercells we observe this issue to be severe because the amount of internal strain is so large for ScAlN alloys that the separate ionic and electronic contributions change quickly (although the total polarization behaves more smoothly).

Therefore, for large changes in polarization, such as that expected from ideal WZ to WZ-like ScAlN, the evolution of the electronic polarization must be carefully monitored for jumps. In Fig. 2 we show the evolution of the three Cartesian components of the SP polarization vector for a $Sc_{12}Al_{52}N_{64}$ supercell, where the transformation from clamped-ion to fully relaxed structure has been characterized in 10 steps: for fixed lattice vectors, the internal atomic positions are linearly scaled from the clamped-ion configuration to the fully relaxed structure. The first observation for this particular structure are the jumps in the electronic polarization for P_x and P_z. If we had naively computed only the end points, as we did for the ionic part in Eq. (12), the results of SP polarization would be wrong (even the wrong sign) for P_x and P_z and only correct for P_y, which presents no jumps in the electronic polarization part. Instead, by monitoring the full transition from ideal WZ to triclinic we can reconstruct the true evolution of the electronic polarization, as shown in the bottom panel of Fig. 2 for the P_z component.

In this context, in order to find a fitting curve one

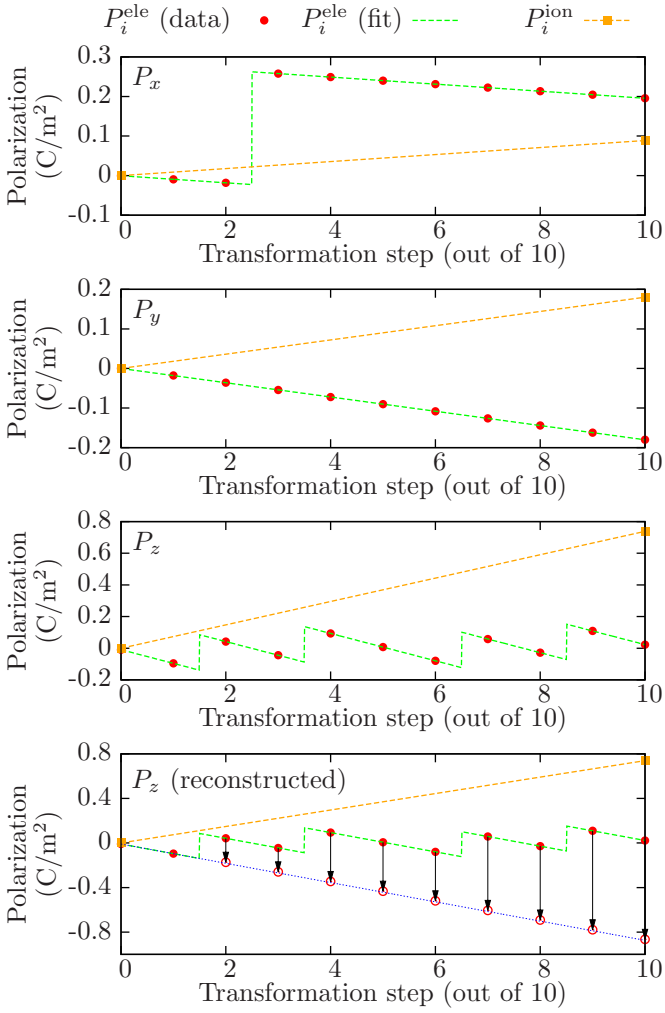

FIG. 2. (Color online) Evolution of the spontaneous polarization vector components during a smooth transformation from the clamped-ion triclinic ScAlN supercell to the fully-relaxed triclinic structure. Example $Sc_{12}Al_{52}N_{64}$ configuration shown.

needs to construct a generalization of a straight line that takes jumps into account. In our implementation, this curve is the following:

$$\begin{aligned} f(\lambda) =& (m\lambda + f_0)\,\text{step\_left}(\lambda, \lambda_1) \\ &+ (m\lambda + f_{N_{\text{jumps}}})\,\text{step\_right}(\lambda, \lambda_{N_{\text{jumps}}}) \\ &+ \sum_{i=1}^{N_{\text{jumps}}-1} (m\lambda + f_i)\,\text{pulse}(\lambda, \lambda_i, \lambda_{i+1}), \end{aligned} \tag{13}$$

where λ is a parameter that characterizes the transformation, in Fig. 2 it would be the step out of 10. f_i are constant vertical shifts and m is the slope of the curve. The different λ_i are the positions of the jumps, ideally chosen to lie in between data points, and N_{jumps} is the total number of jumps: one for P^{ele}_x, none for P^{ele}_y, and 4 for P^{ele}_z in Fig. 2. step_left(λ, λ_i) is a step function, equal to 1 to the left of λ_i and 0 elsewhere. Similarly,

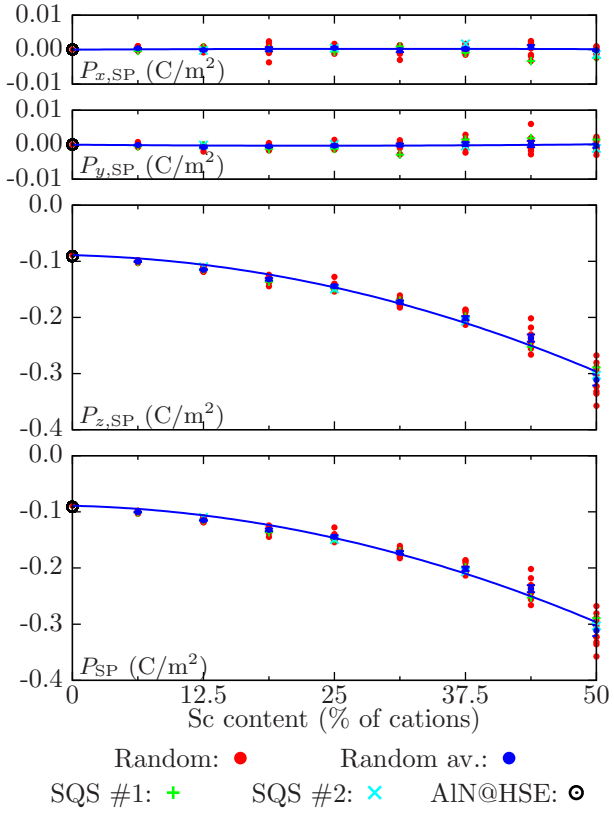

FIG. 3. (Color online) Variation with composition of the spontaneous polarization of random and SQS ScAlN supercells. Average values and quadratic interpolation curve for the random supercells are also given. The values for pure AlN calculated at the HSE level of theory[20] are given for reference.

step_right(λ, λ_i) equals 1 to the right of λ_i and zero elsewhere. Finally, pulse$(\lambda, \lambda_i, \lambda_{i+1})$ is zero everywhere except between two adjacent jumps at λ_i and λ_{i+1} where it equals 1. The (green) dashed lines in Fig. 2 have been generated fitting the f_i and m to the different data sets after identifying the position of the jumps, λ_i. The usefulness of Eq. (13) lies in the fact that it allows to adapt to the irregular shape of the electronic polarization evolution while maintaining the same slope m, irrespective of this shape. Therefore fitting to $f(\lambda)$ produces a single parameter to characterize this evolution: $m = \partial P^{\mathrm{ele}}/\partial\lambda$. Thus, the reconstructed (blue) dotted line in the bottom panel of Fig. 2 is simply $m\lambda + f_0$. The procedure above allows us to systematically process the large amount of data arising from configurational sampling at each composition with the aid of a computer.

Finally, the electronic part of the SP polarization is calculated as follows:

$$P^{\mathrm{ele}}_{i,\mathrm{SP}} = P^{\mathrm{ele}}_{i,\mathrm{idWZ}} + \left(P^{\mathrm{ele}}_{i,\text{ci-tric}} - P^{\mathrm{ele}}_{i,\mathrm{idWZ}}\right) + m_i\delta\lambda, \quad (14)$$

where "ci-tric" refers to the clamped-ion triclinic cell, m_i is the m fitting parameter for each Cartesian component and $\delta\lambda$ is the increment in λ going from the clamped-ion triclinic to the fully relaxed triclinic structures. In Fig. 2 and for all the structures we computed, $\delta\lambda = 10$. The total SP polarization is simply computed as the sum of Eq. (12) and Eq. (14):

$$P_{i,\mathrm{SP}} = P^{\mathrm{ele}}_{i,\mathrm{SP}} + P^{\mathrm{ion}}_{i,\mathrm{SP}}. \quad (15)$$

The results obtained for the different samples and compositions studied are shown in Fig. 3. A small scatter of data can be observed, in particular as the amount of Sc, and therefore the lattice distortion, increases. In the case of SP polarization, the use of SQS instead of configurational sampling of random structures might be justified. Indeed, the SQS values are remarkably close to the averages of random configurations for all compositions. A quadratic fit to the random supercell data yields the following interpolation formula for the SP polarization of $\mathrm{Sc}_x\mathrm{Al}_{1-x}\mathrm{N}$:

$$\begin{aligned} P_{\mathrm{SP}}(x) = &-0.089\,(1-x) - 0.874\,x \\ &+ 0.741\,x\,(1-x)\ \mathrm{C/m^2}. \end{aligned} \quad (16)$$

For consistency with the PZ tensor results from the next section, the SQS results have been left out of the fitting. The expression above has been given in the fashion usually employed for ternary compounds, where it is easy to identify the end values of the binaries and the *bowing* parameter b,[36] which gives the quadratic correction. In the case of ScAlN a large non-linearity with composition of the SP polarization can be observed, with $b = 0.741$ C/m^2 in this case. Note, for comparison, that the SP polarization bowing parameter of the traditional nitride ternaries AlGaN, AlInN and InGaN is one order of magnitude smaller.[37,38] Equation (16) also allows to identify the SP polarization of pure AlN (-0.089 C/m^2) and the (very large) extrapolated value of a hypothetical pure wurtzite ScN (-0.874 C/m^2). The latter is only an artifact of the interpolation procedure and does not bear connection to any real material, since WZ ScN is not stable and high Sc-content ScAlN adopts a hexagonal-layered configuration.[9]

It is worth mentioning that the jumps in the spontaneous polarization introduce a discontinuity in the evolution of the polarization vector that affects the calculation of the PZ tensor through a shift in the reference polarization of the unstrained system. The calculated uncorrected polarization at a (small) finite strain $\mathbf{P}'[\epsilon]$ will belong to the same polarization branch as for $\epsilon = 0$, i.e. the branch at $\lambda = 10$ in the example of Fig. 2. If there have been polarization jumps between the polarization of the ideal structure and that of the unstrained structure, this means that the reconstruction needed for the spontaneous polarization also needs to be carried out for the strained structure. The corrected dipole moment of the unit cell $\mathbf{p}[\epsilon]$ can be related to the uncorrected value $\mathbf{p}'[\epsilon]$ in the following way:

$$\mathbf{p}[\epsilon] = \mathbf{p}'[\epsilon] + (\mathbb{1} + \epsilon)\,(\mathbf{p}_{\mathrm{SP}} - \mathbf{p}'[0])\,, \quad (17)$$

where $\mathbb{1}+\epsilon$ represents a strain transformation applied to the dipole moment vectors. The correct polarization at ϵ is then obtained by dividing Eq. (17) by the unit cell volume at strain ϵ. Note that if there have been no jumps, $\mathbf{p}_{\mathrm{SP}} - \mathbf{p}'[0]$ vanishes and the correction above becomes trivial. One can choose to calculate the uncorrected PZ tensor components e'_{ij} for the given polarization branch and carry out the corrections afterwards, which is arguably a more straightforward route. The corrections are as follows:

$$e_{ij} = \begin{cases} e'_{ij} & \text{if } i = j \text{ or } j = i+3 \\ e'_{ij} - P_{i,\mathrm{SP}} + P'_i[0] & \text{if } i \neq j,\ j = 1,2,3 \\ e'_{ij} + \frac{1}{2}\left(P_{k,\mathrm{SP}} + P'_k[0]\right) & \text{if } j > 3,\ j \neq i+3 \end{cases} \tag{18}$$

where $k = 9 - i - j$. Incidentally, these corrections carry a resemblance to the transformation from improper to proper PZ coefficients[39] that will be discussed in more detail in Sec. IV.

E. Results: piezoelectric tensor

In order to calculate the components of the triclinic PZ tensor of the different supercells, we monitor the evolution of the three Cartesian components of the polarization vector P_i as small strains $\epsilon_j = \pm 0.2$ % are applied.[40] A finite difference calculation then leads to the 18 independent e_{ij}^{tric}. Next, the tensor directly obtained in this way is rotated so as to maximize its hexagonal projection using Eq. (11) and the procedure described in Ref. 34. This allows an optimum hexagonal "alignment" of the tensor. The results for the different configurations and Sc contents are shown in Fig. 4. For clarity of interpretation, the panels in the figure are arranged in the same fashion as the PZ tensor when represented in matrix form, Eq. (3). The vertical scale has been kept fixed for all the PZ coefficients except for e_{33} to enable a direct simultaneous comparison of the magnitude of variation for all the PZ constants. The most immediate observation that can be made is with regards to the large data scattering for different configurations with the same nominal composition. The largest scatter occurs for the hexagonal PZ coefficients e_{15}, e_{31} and e_{33}, but also for e_{16}, e_{21} and e_{22}. Although the latter might seem like an unexpected result, we have previously shown that these components in a wurtzite crystal only vanish as an averaging macroscopic effect, cf. Eq. (14) of Ref. 20. This scatter of results is directly related to the large amount of internal strain that distorts the lattice locally in very different ways for different configurations.

The hexagonal projection of the triclinic PZ tensors in Fig. 4 using Eq. (11) leads to the hexagonal PZ constants of Fig. 5. The composition-dependent expressions from a fit to the random configuration data, given in C/m^2, are:

$$\begin{aligned} e_{15}^{\mathrm{hex}}(x) &= -0.367\,(1-x) - 0.435\,x + 0.417\,x\,(1-x), \\ e_{31}^{\mathrm{hex}}(x) &= -0.424\,(1-x) - 0.286\,x - 0.615\,x\,(1-x), \\ e_{33}^{\mathrm{hex}}(x) &= 1.449\,(1-x) + 8.182\,x - 5.912\,x\,(1-x). \end{aligned} \tag{19}$$

The PBE functional, similar to other local and semilocal DFT functionals, has a number of shortcomings. Using a more expensive approach, for instance a hybrid-functional, better accuracy can be achieved. Running hybrid-functional calculations for the 128-atom supercells is impractical in the present case due to the increased computational cost. A possible approach is to correct the end points for the AlN binary and then follow the same evolution with composition for the alloy as predicted with PBE. Correcting the AlN end values to the HSE hybrid-functional results from Ref. 20, gives significant changes only for e_{31}:

$$\begin{aligned} \tilde{e}_{15}^{\mathrm{hex}}(x) &= -0.39\,(1-x) - 0.458\,x + 0.417\,x\,(1-x), \\ \tilde{e}_{31}^{\mathrm{hex}}(x) &= -0.63\,(1-x) - 0.492\,x - 0.615\,x\,(1-x), \\ \tilde{e}_{33}^{\mathrm{hex}}(x) &= 1.46\,(1-x) + 8.193\,x - 5.912\,x\,(1-x). \end{aligned} \tag{20}$$

We will denote HSE-corrected (cHSE) results with a tilde throughout the rest of the manuscript, meaning in each case that the expressions have been adjusted so that the values for pure AlN match the HSE ones, taken from Refs. 28 and 20 as appropriate. As can be readily seen from the data in Figs. 4 and 5, one cannot rely on the result of SQS calculations alone in order to establish the macroscopic average of the PZ coefficients of ScAlN. Despite being computationally expensive, configurational averaging for random supercells becomes necessary for accurately computing the full PZ tensor (either the triclinic tensor or its hexagonal projection).

Overall, our results indicate a very fast evolution with composition of e_{33} but a smoother behavior for e_{15} and e_{31}. A more detailed discussion of these simulation results in the context of previous theoretical studies and available experimental data, including some own measurements from Sec. III, will be presented in Sec. IV.

F. Elastic constants and piezoelectric moduli

So far we have discussed the values of the piezoelectric coefficients e_{ij} which relate electric polarization and strain ϵ_j:

$$P_i = \sum_{j=1}^{6} e_{ij}\epsilon_j. \tag{21}$$

However, it is not uncommon to describe the piezoelectric response of a material in terms of its piezoelectric moduli d_{ij}, which give the evolution of the electric polarization

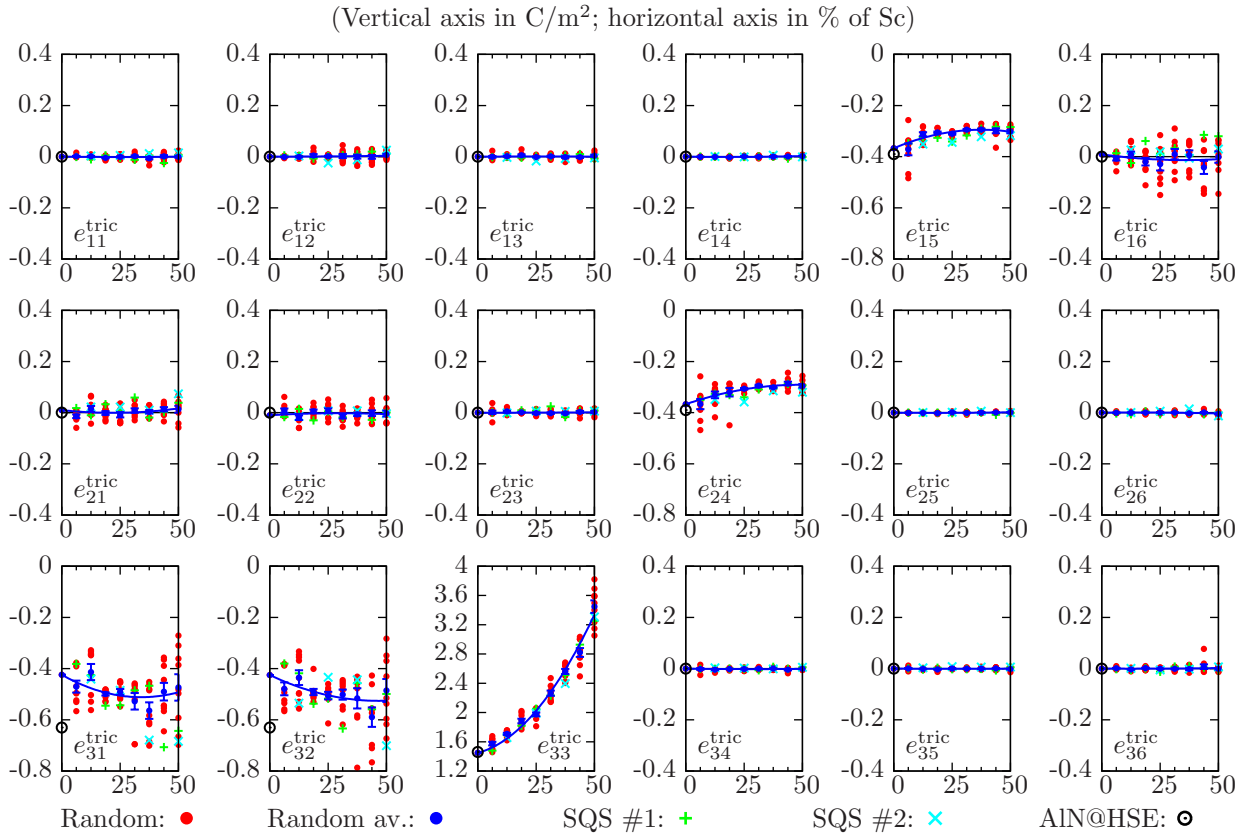

FIG. 4. (Color online) All the components of the triclinic piezoelectric tensor calculated for random and SQS supercells for all the configurations and compositions studied. The quadratic interpolation curves have been fitted to the average random results. The layout follows the appearance of the PZ tensor in matrix representation, Eq. (3).

vector as a function of stress σ_j:

$$P_i = \sum_{j=1}^{6} d_{ij}\sigma_j. \tag{22}$$

The hexagonal tensor of piezoelectric moduli has the same form as that of the piezoelectric constants given in Eq. (4). For completeness and to be able to compare to experimental data on the piezoelectric constants of ScAlN alloys, which is most often given in the literature in terms of the d_{ij}, we compute them too. In order to do so, the elastic constants C_{ij} of ScAlN need to be computed, which can be readily done from the same set of calculations that allow to extract the PZ coefficients. Then, the relation between e_{ij} and d_{ij} can be obtained straightforwardly from the strain-stress relation,

$$\sigma_i = \sum_{j=1}^{6} C_{ij}\epsilon_j, \tag{23}$$

in such a way that the relation between the different PZ coefficients is simply:

$$e_{ij} = \sum_{k=1}^{6} d_{ik}C_{kj}, \qquad d_{ij} = \sum_{k=1}^{6} e_{ik}\left(C^{-1}\right)_{kj}. \tag{24}$$

Given the symmetry of the hexagonal stiffness tensor, the independent non-vanishing hexagonal PZ coefficients and PZ moduli can be expressed as follows:

$$\begin{aligned} &e_{15} = d_{15}C_{44}, \qquad e_{31} = d_{31}(C_{11}+C_{12}) + d_{33}C_{13}, \\ &e_{33} = 2d_{31}C_{13} + d_{33}C_{33}, \end{aligned} \tag{25}$$

for the e_{ij}, and

$$\begin{aligned} &d_{15} = \frac{e_{15}}{C_{44}}, \qquad d_{31} = \frac{e_{31}C_{33} - e_{33}C_{13}}{(C_{11}+C_{12})C_{33} - 2{C_{13}}^2}, \\ &d_{33} = \frac{e_{33}(C_{11}+C_{12}) - 2e_{31}C_{13}}{(C_{11}+C_{12})C_{33} - 2{C_{13}}^2}, \end{aligned} \tag{26}$$

for the d_{ij}. The evolution with composition of the C_{ij} for ScAlN from our simulations is depicted in Fig. 6, where less scatter of data can be observed as compared to the PZ coefficient results. Incidentally, the SQS supercells are also observed to be more suitable for calculating elastic properties of ScAlN than PZ coefficients: the average values for random supercells are very close to the SQS values. The C_{ij} have been obtained following the same procedure outlined in Sec. II C with an optimized rotation of the stiffness tensor followed by a hexagonal projection.[32,34] The projector for the hexagonal stiffness tensor has been previously obtained by Tasnádi *et al.*[41]

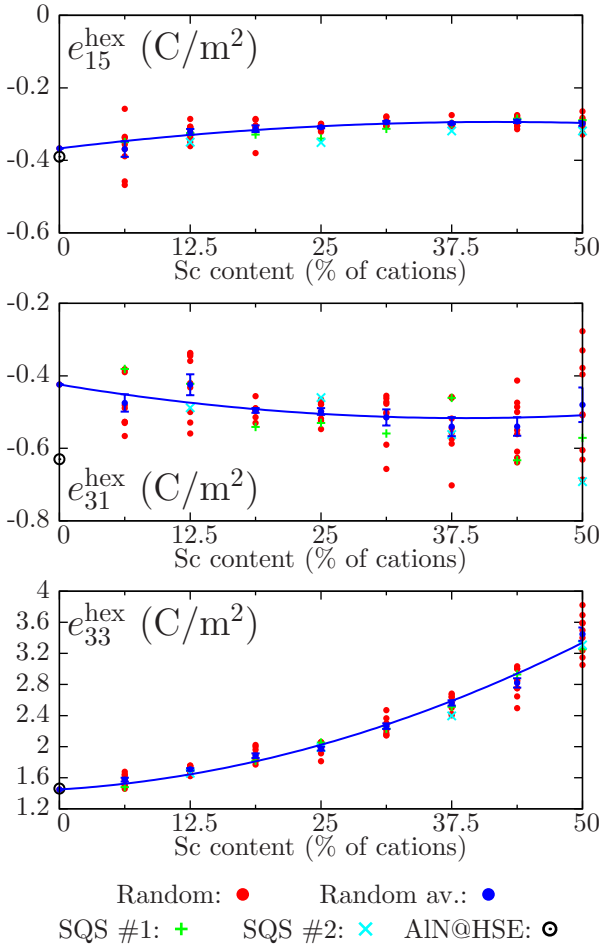

FIG. 5. (Color online) Hexagonal projected components of the triclinic PZ tensor of ScAlN, obtained as explained in detail throughout the text.

The fitted quadratic expressions for the composition-dependent hexagonal elastic constants of $Sc_xAl_{1-x}N$ are:

$$
\begin{aligned}
C_{11}^{\rm hex}(x) &= 378.8\,(1-x) + 263.9\,x - 210.3\,x\,(1-x),\\
C_{12}^{\rm hex}(x) &= 128.9\,(1-x) + 185.1\,x - 61.9\,x\,(1-x),\\
C_{13}^{\rm hex}(x) &= 96.1\,(1-x) + 121.5\,x + 78.9\,x\,(1-x),\\
C_{33}^{\rm hex}(x) &= 357.5\,(1-x) - 51.3\,x - 101.4\,x\,(1-x),\\
C_{44}^{\rm hex}(x) &= 112.4\,(1-x) + 159.0\,x - 137.3\,x\,(1-x),
\end{aligned}
\tag{27}
$$

given in GPa. Underbinding (too long lattice constants) and the correspondingly low elastic constants are well-known shortcomings of generalized-gradient approximations to DFT, including the PBE functional. For this reason, the correction of the C_{ij} to give the right numbers for AlN becomes more critical than in the case of the PZ coefficients. The HSE values for AlN[28] give much better agreement with experiment[42] than the PBE values. The corrected constants (in GPa) are:

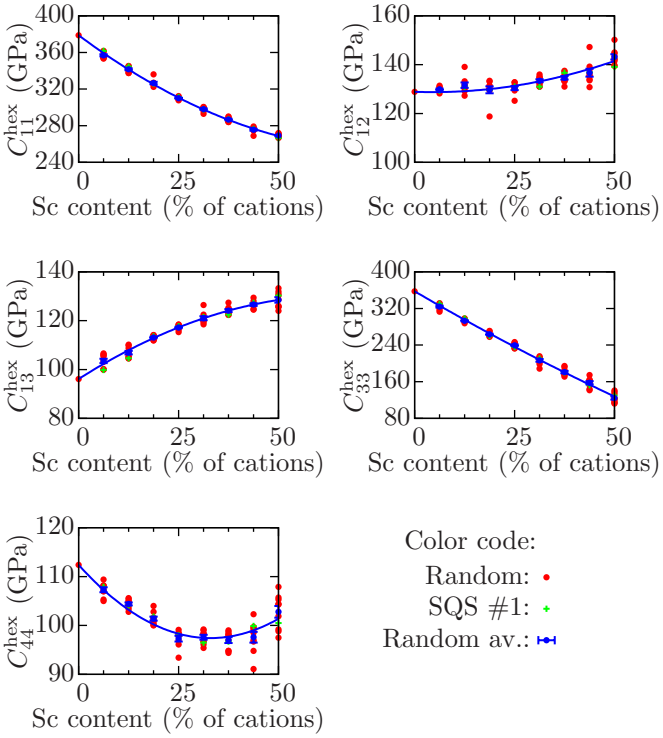

FIG. 6. (Color online) Composition-dependent hexagonal projected components of the stiffness tensor of ScAlN.

$$
\begin{aligned}
\tilde{C}_{11}^{\rm hex}(x) &= 410.2\,(1-x) + 295.3\,x - 210.3\,x\,(1-x),\\
\tilde{C}_{12}^{\rm hex}(x) &= 142.4\,(1-x) + 198.6\,x - 61.9\,x\,(1-x),\\
\tilde{C}_{13}^{\rm hex}(x) &= 110.1\,(1-x) + 135.5\,x + 78.9\,x\,(1-x),\\
\tilde{C}_{33}^{\rm hex}(x) &= 385.0\,(1-x) - 23.8\,x - 101.4\,x\,(1-x),\\
\tilde{C}_{44}^{\rm hex}(x) &= 122.9\,(1-x) + 169.5\,x - 137.3\,x\,(1-x).
\end{aligned}
\tag{28}
$$

Combining Eq. (27) with the expressions in Eq. (19), and Eq. (28) with Eq. (20), for the PBE and HSE-corrected values, respectively, following the relation given by Eq. (26), leads to the following composition-dependent expressions for $d_{ij}^{\rm hex}(x)$ (given in pC/N):

$$
\begin{aligned}
d_{15}^{\rm hex}(x) &= -3.27 + 0.454\,x + 0.869\,x^2 - 0.847\,x^3,\\
d_{31}^{\rm hex}(x) &= -1.784 - 23.0\,x + 149.9\,x^2 - 381\,x^3,\\
d_{33}^{\rm hex}(x) &= 5.01 + 67.3\,x - 458\,x^2 + 1176\,x^3,
\end{aligned}
\tag{29}
$$

for the direct PBE results and

$$
\begin{aligned}
\tilde{d}_{15}^{\rm hex}(x) &= -3.17 + 0.487\,x + 0.660\,x^2 - 0.746\,x^3,\\
\tilde{d}_{31}^{\rm hex}(x) &= -2.14 - 15.09\,x + 78.8\,x^2 - 229\,x^3,\\
\tilde{d}_{33}^{\rm hex}(x) &= 5.02 + 42.3\,x - 238\,x^2 + 704\,x^3,
\end{aligned}
\tag{30}
$$

for the HSE-corrected values. The expressions have been obtained as the best third-order fit to the full expressions

calculated from Eq. (26) (taking Eqs. (19) and (27), and Eqs. (20) and (28) as input) with the constraint that the values for AlN be reproduced exactly. A second-order fit was not enough to correctly describe the evolution with composition of the d_{ij}. Comparison of these results with available literature values will be done in Sec. IV.

III. EXPERIMENTAL MEASUREMENT

Given the more complex setup needed to measure e_{31} and, particularly e_{15}, we carried out measurements of e_{33} at three different compositions using an acoustic wave resonator, in order to be able to partially compare and validate the results of the simulation.

Magnetron sputtering was utilized to fabricate the wurtzite-like ScAlN thin film bulk acoustic wave (BAW) structures.[44] The films in the study were co-sputtered in a von Ardenne CS730S cluster sputtering tool.[45] The ScAl composite sputtering target used consisted of an Al (99.999%) body equipped with Sc (99.9%) pieces. The number of Sc pellets on the target determines the chemical composition of the grown films, which was analyzed using time-of-flight elastic recoil detection analysis (ToF-ERDA).[46–48] The BAW resonator structure used to extract the e_{33} piezoelectric coefficient is made up of a ScAlN plate between metal electrodes which was deposited onto an acoustic Bragg reflector consisting of two pairs of SiO_2/W layers with a quarter wavelength thickness. A voltage source is connected across the thickness dimension of the piezolayer, which we denote z. Wafer level S-parameter measurements were performed with a Hewlett-Packard 8720D vector network analyzer.

The one-dimensional description of the resonator is as follows. The wave equation for the mechanical displacement u along z is

$$\frac{\partial^2 u}{\partial t^2} = v_D \frac{\partial^2 u}{\partial z^2}, \tag{31}$$

where v_D is the sound phase velocity under the prevailing conditions. If the effective stiffness of the material is C^D and the mass density is ρ, the velocity is given by

$$v_D = \sqrt{\frac{c^D}{\rho}}. \tag{32}$$

We search an analytic harmonic solution of the equation

$$\frac{\partial^2 u}{\partial z^2} = -k^2\, u, \tag{33}$$

in a multilayer structure in the form

$$u_i = A_i \mathrm{e}^{-\mathrm{i}k_i z} + B_i \mathrm{e}^{\mathrm{i}k_i z}, \tag{34}$$

where $k_i = \omega/v_i$ is the wave number in layer i. The amplitude coefficients A_i and B_i are determined from the boundary conditions establishing that the stress and displacement are continuous across each interface. The electric field in the piezolayer is

$$E = \frac{J_i}{\mathrm{i}\omega\varepsilon_i} - h_i \frac{\partial u}{\partial z}, \tag{35}$$

where h_i is the piezoelectric coefficient, ε_i the electrical permittivity and J_i the current density through layer i at angular frequency ω. The voltage U of the device is obtained by integrating the field E over the thickness, and the current I by integrating J over the electrode area. Finally, the impedance is calculated as $Z = U/I$. From the measured impedance the following quantities are calculated: i) the parallel capacitance C_0, which is used to calculate the permittivity, ii) the phase

$$\varphi = \arctan\left(\frac{\mathrm{Im}\{Z\}}{\mathrm{Re}\{Z\}}\right), \tag{36}$$

and iii) the quality factor

$$Q = \frac{\omega}{2}\left|\frac{\mathrm{d}\varphi}{\mathrm{d}\omega}\right|. \tag{37}$$

The resonance frequencies f_s and f_p are then determined as the frequencies of the maximum values of Q. The electromechanical coupling coefficient is given by

$$k_{\mathrm{eff}} = \sqrt{1 - \left(\frac{f_s}{f_p}\right)^2}. \tag{38}$$

Finally, the piezoelectric coefficient $e_{33} = \varepsilon^T h$ is chosen so that the measured and calculated k_{eff} are equal. The values of e_{33} together with the different material parameters obtained for the three ScAlN samples studied are given in Table I.

IV. DISCUSSION, SUMMARY AND CONCLUSIONS

Before comparing results from simulation and experiment it is worth making the distinction between proper and improper PZ coefficients. A more detailed discussion is available from the paper by Vanderbilt[39] and references therein. The "improper" coefficients, that we have calculated in Sec. II E, link the electric polarization vector and strain through Eq. (21), and can be alternatively expressed as

$$e_{ij} = \frac{\partial P_i}{\partial \epsilon_j}. \tag{39}$$

The "proper" PZ coefficient, on the other hand, links the adiabatic change in current density $\mathbf{J}$ in response to a slow deformation $\dot{\epsilon_j} = \mathrm{d}\epsilon_j/\mathrm{d}t$:[39]

$$e^{\mathrm{p}}_{ij} = \frac{\partial J_i}{\partial \dot{\epsilon_j}}, \tag{40}$$

TABLE I. Parameters involved in the experimental determination of e_{33} used in this work. The density values are calculated from the lattice constants measured by Matloub *et al.*[43] and the atomic masses of Sc, Al and N. Note: the elastic constant C_{33} is chosen so that the calculated resonance frequency is close to the measured value.

	Measured	Calculated	Measured	Calculated	Measured	Calculated
Sample	GB177E13		HCScAlN_J07R10		EHC_D04_R09	
Sc content (% of cations)	0%		14%		26%	
Thickness (nm)	1270		1070		1010	
Relative permittivity ε	9.37	9.37	10.68	10.68	13.06	13.06
e_{33} (C/m^2)		1.46		1.81		2.333
Density (g/cm^3)		3.512		3.530		3.560
C_{33} (GPa)		379.9		340		300
f_s (MHz)	1969.5	1942.2	1886.6	1856.2	1753.2	1700.7
f_p (MHz)	2023.3	1996.0	1966.4	1934.8	1872.9	1816.8
k_{eff}	0.229	0.2306	0.282	0.2822	0.352	0.3517
C_0 (pF)	5.302	5.302	1.862	1.86	1.869	1.87

where J_i indicates current density along direction i (in contrast to Eq. (35), where i denotes layer and the current density is assumed to flow along the polar axis). The definitions in Eqs. (39) and (40) lead in general to different PZ coefficients. The transformation between improper and proper PZ coefficients for the three independent wurtzite e_{ij} is as follows:[49]

$$\begin{aligned} e^{\text{p}}_{15} &= e_{15} - \frac{1}{2}P_{3,\text{SP}}, \\ e^{\text{p}}_{31} &= e_{31} + P_{3,\text{SP}}, \\ e^{\text{p}}_{33} &= e_{33}. \end{aligned} \tag{41}$$

The improper coefficient is the relevant one when calculating polarization charges, for instance interfacial charge accumulation at quantum well interfaces.[50] The proper coefficient, on the other hand, is the quantity that should be compared to experiments where PZ coefficients are measured in terms of flowing currents.[39] For systems with small spontaneous polarization the corrections can be negligible, but in view of the fact that the spontaneous polarization of ScAlN becomes of the same order of magnitude as the PZ coefficients for large Sc fraction, the corrections in Eq. (41) become important. Therefore, we report the different proper coefficients here, as obtained from applying the corrections of Eq. (41) to the different expressions of the previous sections. The *proper* PZ coefficients e_{ij} directly obtained from the PBE results are:

$$\begin{aligned} e^{\text{p}}_{15}(x) &= -0.323\,(1-x) + 0.002\,x + 0.047\,x\,(1-x), \\ e^{\text{p}}_{31}(x) &= -0.513\,(1-x) - 1.160\,x + 0.126\,x\,(1-x), \\ e^{\text{p}}_{33}(x) &= e_{33}(x), \end{aligned} \tag{42}$$

where $e_{33}(x)$ is taken from Eq. (19). For the HSE-corrected values, the proper e_{ij} become:

$$\begin{aligned} \tilde{e}^{\text{p}}_{15}(x) &= -0.346\,(1-x) - 0.021\,x + 0.047\,x\,(1-x), \\ \tilde{e}^{\text{p}}_{31}(x) &= -0.719\,(1-x) - 1.366\,x + 0.126\,x\,(1-x), \\ \tilde{e}^{\text{p}}_{33}(x) &= \tilde{e}_{33}(x). \end{aligned} \tag{43}$$

where $\tilde{e}_{33}(x)$ is taken from Eq. (20). The proper PZ moduli from PBE and HSE-corrected calculations are

$$\begin{aligned} d^{\text{p}}_{15}(x) &= -2.87 + 0.862\,x + 5.35\,x^2 - 2.89\,x^3, \\ d^{\text{p}}_{31}(x) &= -1.979 - 24.3\,x + 156.9\,x^2 - 403\,x^3, \\ d^{\text{p}}_{33}(x) &= 5.12 + 70.8\,x - 485\,x^2 + 1243\,x^3, \end{aligned} \tag{44}$$

and

$$\begin{aligned} \tilde{d}^{\text{p}}_{15}(x) &= -2.81 + 0.846\,x + 4.63\,x^2 - 2.40\,x^3, \\ \tilde{d}^{\text{p}}_{31}(x) &= -2.32 - 15.90\,x + 82.0\,x^2 - 243\,x^3, \\ \tilde{d}^{\text{p}}_{33}(x) &= 5.12 + 44.4\,x - 253\,x^2 + 745\,x^3, \end{aligned} \tag{45}$$

respectively. Note that unlike for the PZ coefficient, the proper PZ modulus d^{p}_{33} is *not* equal to the improper one because both e^{p}_{33} and e^{p}_{31} are involved in its determination [cf. Eq. (26)].

In Fig. 7 we show a comparison of the present results and available experimental and simulation data from the literature. Most of the available data is for the d_{ij}, rather than the e_{ij}. In particular, there is lack of published data regarding the shear PZ coefficient e_{15} and shear PZ modulus d_{15}, for which this work seems to be the first one to report values. In addition, although e_{31} could be estimated from available values of PZ moduli and elastic constants, there does not seem to be any explicit reports for this coefficient either. Matloub *et al.*[43] have reported values for the "effective transverse" $e_{31,\text{f}}$ which, attending to the definition provided by the authors in previous work,[51] should relate to e_{31} as $e_{31} = e_{31,\text{f}} + \frac{C_{13}e_{33}}{C_{33}}$. Therefore we use our calculated values of C_{13}, C_{33} and e_{33} to

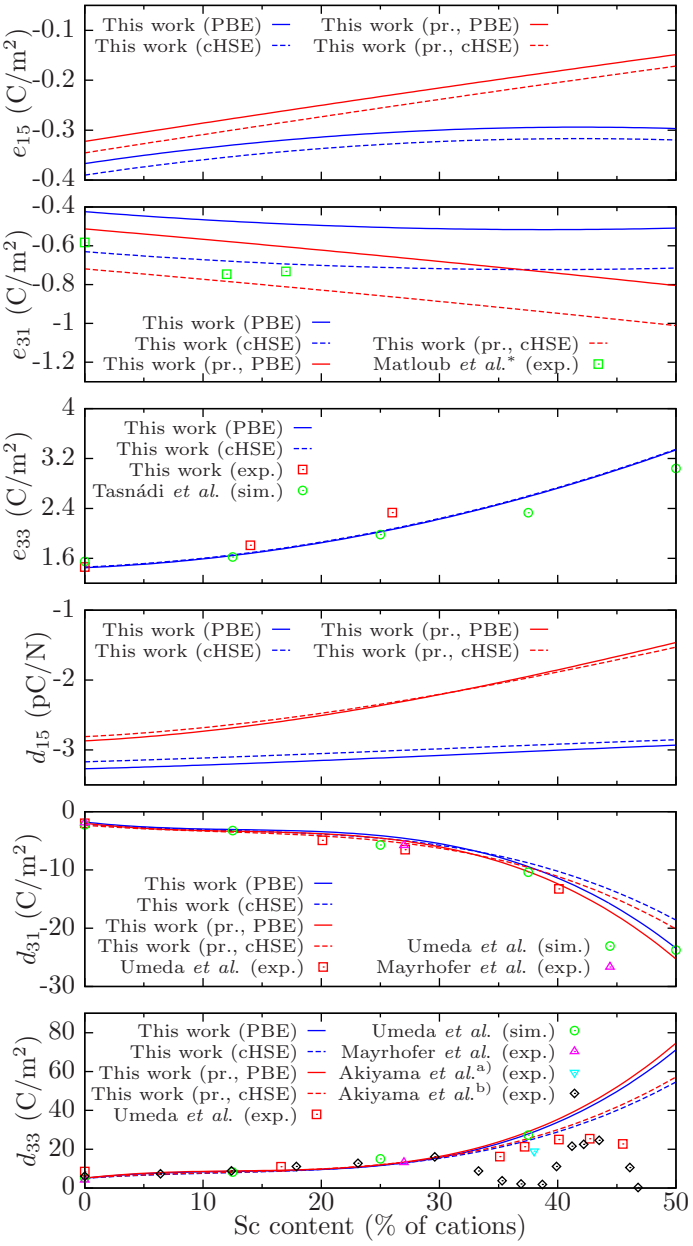

FIG. 7. (Color online) Comparison of the present results ("pr." stands for "proper") and available literature data, taken from: Matloub *et al.*[43] (data modified for comparison [see text], experiment); Tasnádi *et al.*[9] (simulation); Umeda *et al.*[7] (simulation & experiment); Mayrhofer *et al.*[8] (experiment); Akiyama *et al.* a)[6] (experiment); and Akiyama *et al.* b)[5] (experiment). See text for a discussion.

be able to compare to their experimental results. Unfortunately, the relation between electric polarization and stress has a much more extreme dependence on composition for ScAlN alloys due to the lattice softening along the c axis as the Sc fraction increases,[9,33] if compared to the relation between polarization and strain. This translates into the very rapid variation with composition of d_{31} and d_{33} beyond $x \approx 30\%$. It is then more difficult to disentangle the contributions to electric polarization arising from a) crystal deformation and b) lattice softening when looking at the PZ moduli. This also means that any uncertainty relating to the knowledge of the elastic constants has a strong impact on the derivation of the d_{ij} values. In contrast, the relation between crystal deformation and polarization is more transparent when looking at the PZ coefficients e_{ij}, which preserve a smoother behavior throughout the full compositional regime studied.

Overall, the agreement with previous simulations is difficult to establish due to the fact that both available studies, by Tasnádi *et al.*[9] and Umeda *et al.*[7] did not consider configurational sampling, which we have shown to affect the results. The agreement is good between our calculations and Tasnádi's results of e_{33}, obtained using 128-atom SQS supercells, for moderate and low Sc content. For higher Sc content the spread of e_{33} values increases, meaning that a single SQS supercell per composition is not enough to capture the effects of configurational disorder. The agreement between the simulation results of Umeda *et al.*[7] and the present work is not too bad for d_{31} but less good for d_{33}. Umeda used small 32-atom supercells for which the spurious effects of periodicity and artificial alloy order (the structures were generated maximizing the inter-Sc distances) might have influenced the results.

With regards to agreement with experiment, the only experimental values for e_{ij} reported so far seem to be the e_{33} values of the present study, which our simulations slightly underestimate. The e_{31} values from Matloub *et al.*,[43] extracted from their $e_{31,\mathrm{f}}$ as outlined previously, show reasonable agreement with our calculations. Reported values for d_{31} and especially d_{33} are more abundant. Our results seem to be in good agreement with d_{31} and in reasonably good agreement for d_{33} over more or less the full compositional range, especially in the case of the HSE-corrected results. Note that the dips of Akiyama's values[5] at around 37% Sc content and beyond 45% Sc content, as well as Umeda's values[7] dip beyond 40% Sc content, are likely due to deteriorating crystal quality.[5,10] Note that in every case discussed above, it should be the proper ("pr." on the graph) PZ coefficient to be compared to the experimental value.

The largest sources of error in experimental measurement are i) those intrinsic to the experimental setup and ii) those due to the lack of knowledge of the ScAlN alloy properties, in particular elastic properties (which are usually measured simultaneously with the PZ coefficients) and the amount of incorporated Sc. Due to the discussed lattice softening that takes over rapidly as the Sc content increases, the lack of accurately-determined elastic properties is likely the largest source of error in experimental measurements. A further source of experimental uncertainty is related to the microscopic structure of the alloy, including the possible effect of clustering, and how it affects the PZ properties of the material. In particular, Akiyama *et al.* showed that the alloy microstructure, which is influenced by Sc content and growth tem-

perature, affects the PZ performance of ScAlN films.[52] Zukauskaite *et al.* have also shown that formation of Al-rich and Sc-rich domains can occur under unfavorable growth conditions at high temperature and high Sc concentrations but should not happen for films grown at lower temperature and lower Sc contents.[53] Therefore, clustering might be directly or indirectly linked to deteriorating PZ properties of ScAlN for low crystalline quality samples (see for instance the dip of Akiyama's results for d_{33} in Fig. 7) but, otherwise, the assumption of a random alloy for the present simulations should be representative of high crystalline quality experimental samples. The effect of clustering on the simulation results could be an interesting topic to be explored in future studies.

From the simulation, errors arise from two main fronts: i) the effect of finite-size supercells and configurational disorder which we have thoroughly shown in Sec. II to have an impact on the results; ii) the inaccuracy introduced by the choice of DFT functional. We argue that, in order to address the first issue, configurational sampling is required, as evidenced by the large spread of data displayed in Fig. 4. Even if the number of configurations used (9 random supercells per composition) is not enough to accurately determine the PZ tensor at a single composition, the combined effect of all the available data points through the whole compositional regime leads to a much improved fitting of interpolation formulas. This is evidenced by the fact that the fitting curves for the non-hexagonal components of the triclinic PZ tensor are close to zero, even for those with larger spread (e_{16}, e_{21} and e_{22}). We could have attempted to compute more values for each composition, however from a practical point of view such a study becomes computationally too expensive.[54] The second issue is more difficult to address. A good benchmark for the performance of DFT functionals for semiconductors is the HSE hybrid functional,[55] as already discussed. While it performs considerably better than LDA and GGA functionals with respect to prediction of elastic and structural properties,[56] it has been previously shown that with regards to calculation of spontaneous and piezoelectric polarization the main differences with other functionals lie in the description and impact of internal strain on the results.[20] Given the large internal strain present in ScAlN, this is probably the main source of error in our simulation results. To account for this, given the computational limitations to carrying out hybrid-functional calculations for large systems, we have corrected the expressions for the PZ coefficients so that the AlN end points are described according to the HSE results. The goodness of this approximation relies on how well the trends with composition are described by the PBE functional.

Taking all these concerns into consideration, we recommend the use of Eqs. (16), (20), (28) and (30) for the composition-dependent values of the spontaneous polarization, the piezoelectric coefficients e_{ij}, the elastic constants C_{ij} and the piezoelectric moduli d_{ij}, respectively, of ScAlN alloys. For the "proper" PZ coefficients e^{p}_{ij} and moduli d^{p}_{ij} we recommend Eqs. (43) and (45), respectively.

ACKNOWLEDGMENTS

Computational resources for the present study were provided by Aalto University's Science-IT project through the Triton cluster, and by CSC – IT Center for Science through the Sisu supercomputer. The authors would like to thank Kenichiro Mizohata from Helsinki University for the ToF-ERDA measurements.

Appendix: Relation between randomness and PZ coefficient

Given the observed result that SQS cells do not reproduce the average piezoelectric constants of ScAlN as well as they do reproduce other properties, we have attempted to study whether there is any correlation between supercell randomness and the calculated piezoelectric coefficients. The results of this study are presented in Fig. 8. The pair-correlation coefficients of an ideally random alloy are minimal in absolute value for all nearest-neighbor shells, and so SQS supercells are generated by placing the different atoms so that these coefficients are minimized.[18] The lack of any obvious trend between the "randomness"

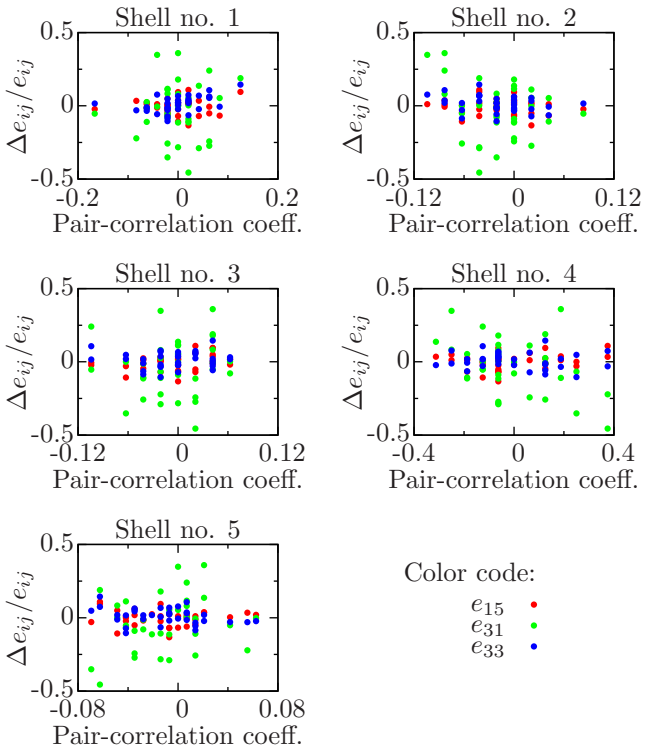

FIG. 8. (Color online) Deviation from the interpolation formulas for e_{ij} versus pair-correlation coefficients of the random ScAlN supercells up to the 5th shell.

of the random supercells and their ability to yield PZ coefficients close to the average values then explains, at least in part, why SQSs are not able to produce representative results consistently. Note that this is in contrast to the situation for elastic constants, where SQSs yield values in good agreement with average results (Fig. 6).

* mcaroba@gmail.com

[1] M. R. Krames, O. B. Shchekin, R. Mueller-Mach, G. O. Mueller, L. Zhou, G. Harbers, and M. G. Craford, "Status and future of high-power light-emitting diodes for solid-state lighting," J. Disp. Technol. **3**, 160 (2007).

[2] C. J. Humphreys, "Solid-state lighting," MRS Bull. **33**, 459 (2008).

[3] M. A. Moram, Y. Zhang, M. J. Kappers, Z. H. Barber, and C. J. Humphreys, "Dislocation reduction in gallium nitride films using scandium nitride interlayers," Appl. Phys. Lett. **91**, 152101 (2007).

[4] M. A. Moram, Y. Zhang, T. B. Joyce, D. Holec, P. R. Chalker, P. H. Mayrhofer, M. J. Kappers, and C. J. Humphreys, "Structural properties of wurtzitelike ScGaN films grown by NH_3-molecular beam epitaxy," J. Appl. Phys. **106**, 113533 (2009).

[5] M. Akiyama, T. Kamohara, K. Kano, A. Teshigahara, Y. Takeuchi, and N. Kawahara, "Enhancement of piezoelectric response in scandium aluminum nitride alloy thin films prepared by dual reactive cosputtering," Adv. Mater. **21**, 593 (2009).

[6] M. Akiyama, T. Tabaru, K. Nishikubo, A. Teshigahara, and K. Kano, "Preparation of scandium aluminum nitride thin films by using scandium aluminum alloy sputtering target and design of experiments," J. Ceram. Soc. Jap. **118**, 1166 (2010).

[7] K. Umeda, H. Kawai, A. Honda, M. Akiyama, T. Kato, and T. Fukura, "Piezoelectric properties of ScAlN thin films for piezo-MEMS devices," in *Micro Electro Mechanical Systems (MEMS), 2013 IEEE 26th International Conference on* (IEEE, 2013) p. 733.

[8] P. M. Mayrhofer, H. Euchner, A. Bittner, and U. Schmid, "Circular test structure for the determination of piezoelectric constants of $Sc_xAl_{1-x}N$ thin films applying laser doppler vibrometry and FEM simulations," Sensor. Actuat. A: Phys. **222**, 301 (2014).

[9] F. Tasnádi, B. Alling, C. Höglund, G. Wingqvist, J. Birch, L. Hultman, and I. A. Abrikosov, "Origin of the anomalous piezoelectric response in wurtzite $Sc_xAl_{1-x}N$ alloys," Phys. Rev. Lett. **104**, 137601 (2010).

[10] M. A. Moram and S. Zhang, "ScGaN and ScAlN: emerging nitride materials," J. Mater. Chem. A **2**, 6042 (2014).

[11] P. Hohenberg and W. Kohn, "Inhomogeneous electron gas," Phys. Rev. **136**, B864 (1964).

[12] W. Kohn and L. J. Sham, "Self-consistent equations including exchange and correlation effects," Phys. Rev. **140**, A1133 (1965).

[13] D. Vanderbilt and R. D. King-Smith, "Electric polarization as a bulk quantity and its relation to surface charge," Phys. Rev. B **48**, 4442 (1993).

[14] R. D. King-Smith and D. Vanderbilt, "Theory of polarization of crystalline solids," Phys. Rev. B **47**, 1651 (1993).

[15] R. Resta, "Macroscopic polarization in crystalline dielectrics: the geometric phase approach," Rev. Mod. Phys. **66**, 899 (1994).

[16] R. Resta and D. Vanderbilt, "Physics of ferroelectrics: a modern perspective," (Springer-Verlag, Berlin Heidelberg, 2007) Chap. Theory of Polarization: A Modern Approach.

[17] F. Bernardini, V. Fiorentini, and D. Vanderbilt, "Spontaneous polarization and piezoelectric constants of III-V nitrides," Phys. Rev. B **56**, 10024 (1997).

[18] S.-H. Wei, L. G. Ferreira, J. E. Bernard, and A. Zunger, "Electronic properties of random alloys: Special quasirandom structures," Phys. Rev. B **42**, 9622 (1990).

[19] S. Zhang, D. Holec, W. Y. Fu, C. J. Humphreys, and M. A. Moram, "Tunable optoelectronic and ferroelectric properties in Sc-based III-nitrides," J. Appl. Phys. **114**, 133510 (2013).

[20] M. A. Caro, S. Schulz, and E. P. O'Reilly, "Theory of local electric polarization and its relation to internal strain: Impact on polarization potential and electronic properties of group-III nitrides," Phys. Rev. B **88**, 214103 (2013).

[21] G. Kresse and J. Furthmüller, "Efficient iterative schemes for *ab initio* total-energy calculations using a plane-wave basis set," Phys. Rev. B **54**, 11169 (1996).

[22] Vienna *Ab initio* Simulation Package (VASP), [http://www.vasp.at], see also on line documentation.

[23] P. E. Blöchl, "Projector augmented-wave method," Phys. Rev. B **50**, 17953 (1994).

[24] G. Kresse and D. Joubert, "From ultrasoft pseudopotentials to the projector augmented-wave method," Phys. Rev. B **59**, 1758 (1999).

[25] J. P. Perdew, K. Burke, and M. Ernzerhof, "Generalized gradient approximation made simple," Phys. Rev. Lett. **77**, 3865 (1996).

[26] H. J. Monkhorst and J. D. Pack, "Special points for Brillouin-zone integrations," Physical Review B **13**, 5188 (1976).

[27] Q. Yan, P. Rinke, M. Scheffler, and C. G. Van de Walle, "Strain effects in group-III nitrides: Deformation potentials for AlN, GaN, and InN," Appl. Phys. Lett. **95**, 121111 (2009).

[28] M. A. Caro, S. Schulz, and E. P. O'Reilly, "Hybrid functional study of the elastic and structural properties of wurtzite and zinc-blende group-III nitrides," Phys. Rev. B **86**, 014117 (2012).

[29] M. A. Caro, S. Schulz, and E. P. O'Reilly, "Comparison of stress and total energy methods for calculation of elastic properties of semiconductors," J. Phys.: Condens. Matter **25**, 025803 (2013).

[30] For a practical example see, for instance, M. A. Caro, *Theory of elasticity and electric polarization effects in the group-III nitrides*, Ph.D. thesis, University College Cork (2013).

[31] J. F. Nye, *Physical properties of crystals: their representation by tensors and matrices* (Oxford University Press, Oxford, 1985).

[32] M. Moakher and A. N Norris, "The closest elastic tensor of arbitrary symmetry to an elasticity tensor of lower symmetry," J. Elasticity **85**, 215 (2006).

[33] S. Zhang, W. Y. Fu, D. Holec, C. J. Humphreys, and M. A. Moram, "Elastic constants and critical thicknesses of ScGaN and ScAlN," J. Appl. Phys. **114**, 243516 (2013).

[34] M. A. Caro, "Extended scheme for the projection of material tensors of arbitrary symmetry onto a higher symmetry tensor," arXiv:1408.1219.

[35] In general, the hexagonal projection could be plus or minus the norm of the triclinic spontaneous polarization vector. However, for wurtzite materials in the usual representation the spontaneous polarization value along the polar axis has negative sign. Therefore, if the triclinic cell is well "aligned" with the underlying hexagonal lattice, the rotation angles can be taken to be the smallest possible set, and the corresponding hexagonal projection of the spontaneous polarization is negative.

[36] See, for instance, I. Vurgaftman, J. R. Meyer, and L. R. Ram-Mohan, "Band parameters for III-V compound semiconductors and their alloys," J. Appl. Phys. **89**, 5815 (2001).

[37] F. Bernardini and V. Fiorentini, "Nonlinear macroscopic polarization in III-V nitride alloys," Phys. Rev. B **64**, 085207 (2001).

[38] V. Fiorentini, F. Bernardini, and O. Ambacher, "Evidence for nonlinear macroscopic polarization in III-V nitride alloy heterostructures," Appl. Phys. Lett. **80**, 1204 (2002).

[39] D. Vanderbilt, "Berry-phase theory of proper piezoelectric response," J. Phys. Chem. Solids **61**, 147 (2000).

[40] We have verified that this amount of strain is sufficiently small to ensure we are well within the linear regime, but large enough that the numerical noise does not impact the results – a calculation with $\epsilon_j = \pm 0.5$ % yielded basically the same PZ tensor for a test configuration.

[41] See Supplemental Information from F. Tasnádi, M. Odén, and I. A. Abrikosov, "*Ab initio* elastic tensor of cubic $Ti_{0.5}Al_{0.5}N$ alloys: Dependence of elastic constants on size and shape of the supercell model and their convergence," Phys. Rev. B **85**, 144112 (2012).

[42] L. E. McNeil, M. Grimsditch, and R. H. French, "Vibrational spectroscopy of aluminum nitride," J. Am. Ceram. Soc. **76**, 1132 (1993).

[43] R. Matloub, M. Hadad, A. Mazzalai, N. Chidambaram, G. Moulard, C. S. Sandu, Th. Metzger, and P. Muralt, "Piezoelectric $Al_{1-x}Sc_xN$ thin films: A semiconductor compatible solution for mechanical energy harvesting and sensors," Appl. Phys. Lett. **102**, 152903 (2013).

[44] See, for instance, S. Mahon and R. Aigner, "Bulk acoustic wave devices–why, how, and where they are going," in *CS MANTECH Conference* (2007) p. 15.

[45] T. Riekkinen, A. Nurmela, J. Molarius, T. Pensala, P. Kostamo, M. Ylilammi, and S. van Dijken, "Influence of the seed layer on structural and electro-acoustic properties of sputter-deposited AlN resonators," Thin Solid Films **517**, 6588 (2009).

[46] J. L'Ecuyer, C. Brassard, C. Cardinal, J. Chabbal, L. Deschenes, J. P. Labrie, B. Terreault, J. G. Martel, and R. St.-Jacques, "An accurate and sensitive method for the determination of the depth distribution of light elements in heavy materials," J. Appl. Phys. **47**, 381 (1976).

[47] J. Jokinen, J. Keinonen, P. Tikkanen, A. Kuronen, T. Ahlgren, and K. Nordlund, "Comparison of TOF-ERDA and nuclear resonance reaction techniques for range profile measurements of keV energy implants," Nucl. Instrum. Meth. B **119**, 533 (1996).

[48] K. Mizohata, *Progress in Elastic Recoil Detection Analysis*, Ph.D. thesis, Helsinki University (2012).

[49] The expression for e_{15} differs from Vanderbilt's[39] by a factor of 2 because Vanderbilt allowed for an antisymmetric part in the strain tensor. Once the symmetry of the strain tensor upon exchange of the Cartesian indices is considered, $\epsilon_{ij} = \epsilon_{ji}$, the expression that arises for $e_{15} \equiv e_{113} = e_{131}$ is the one given by us.

[50] F. Bernardini, V. Fiorentini, and D. Vanderbilt, "Accurate calculation of polarization-related quantities in semiconductors," Phys. Rev. B **63**, 193201 (2001).

[51] M.-A. Dubois and P. Muralt, "Measurement of the effective transverse piezoelectric coefficient e_{31}, f of AlN and $Pb(Zr_x,Ti_{1-x})O_3$ thin films," Sensor. Actuat. A-Physical **77**, 106 (1999).

[52] M. Akiyama, K. Kano, and A. Teshigahara, "Influence of growth temperature and scandium concentration on piezoelectric response of scandium aluminum nitride alloy thin films," Appl. Phys. Lett. **95**, 162107 (2009).

[53] A. Zukauskaite, G. Wingqvist, J. Palisaitis, J. Jensen, P. O. Å. Persson, R. Matloub, P. Muralt, Y. Kim, J. Birch, and L. Hultman, "Microstructure and dielectric properties of piezoelectric magnetron sputtered w-$Sc_xAl_{1-x}N$ thin films," J. Appl. Phys. **111**, 093527 (2012).

[54] We employed a total of circa 0.5 million CPU hours on the random supercell calculations, approximately equal to a single-core computer running uninterruptedly for 60 years.

[55] J. Heyd, G. E. Scuseria, and M. Ernzerhof, "Hybrid functionals based on a screened Coulomb potential," J. Chem. Phys. **118**, 8207 (2003).

[56] J. Paier, M. Marsman, K. Hummer, G. Kresse, I. C. Gerber, and J. G. Angyan, "Screened hybrid density functionals applied to solids," J. Chem. Phys. **124**, 154709 (2006).